Growth optimization of single-phase novel colloidal perovskite $Cs_3Bi_2I_9$ nanocrystals and $Cs_3Bi_2I_9@SiO_2$ core-shell nanocomposites for bio-medical application

Santhana Vedi,[a] Thangaraju Dheivasigamani,[a] Govarthini Seerangan Selvam,[a] Takashi Kawakami,[b] Narmadha Rajeswaran,[c] Selvakumar Rajendran,[c] Alagar Muthukaruppan[d], F. Maiz[e,f], Mohd. Shkir*[e,g]*

[a]nano-*crystal Design and Application Lab (n-DAL), Department of Physics, PSG Institute of Technology and Applied Research, Coimbatore-641062, Tamil Nadu, India.*

[b]*Faculty of Life and Environmental Sciences, Graduate Faculty of Interdisciplinary Research, University of Yamanashi, 4-4-37 Takeda, Kofu, Yamanashi, 400-8510, Japan*

[c]*Tissue Engineering Laboratory, PSG Institute of Advanced Studies, Coimbatore, Tamil Nadu, India*

[d]*Polymer Engineering Lab (PEL), PSG Institute of Technology and Applied Research, Coimbatore-641062, Tamil Nadu, India.*

[e]*Department of Physics, Faculty of Science, King Khalid University, P.O. Box 9004, Abha 61413, Saudi Arabia*

[f]*Laboratory of Thermal Processes, Center for Energy Research and Technology, Borj-Cedria, BP: 95, Tunisia.*

[g]*Department of Chemistry and University Centre for Research & Development, Chandigarh University, Mohali-140413, Punjab*

*Corresponding author Dheivasigamani Thangaraju

E-mail: shkirphysics@gmail.com; dthangaraju@gmail.com

Abstract:

Lead-free halide perovskites have gained attention in recent years as a viable material with distinctive characteristics than other conventional semiconductor materials. Lead-free $Cs_3Bi_2I_9$ colloidal perovskite nanocrystals is chosen for eliminating synthesis difficulty and implementation bioimaging applications. The nano-structured $Cs_3Bi_2I_9$ perovskite composites were coated with a thin coating of SiO_2 by *in-situ* tetraethyl orthosilicate (TEOS)/(3-Aminopropyl) Trimethoxysilane injection growth method to enhance its stability in aqueous medium and bio-compatibility. Single-phase novel $Cs_3Bi_2I_9$ colloidal perovskite nanocrystal synthesis was successfully developed and optimized by adopting different synthetic conditions with varied experimental parameters, viz., the stoichiometric ratio of precursor compounds, growth temperature, and period. The characterization studies, including X-Ray Diffractometry (XRD) and Transmission Electron Microscopy (TEM), confirm the hexagonal structure of $Cs_3Bi_2I_9$ and their cubic morphology. A broad emission peak at the red region was captured for pure and composite perovskite under different excitation wavelengths and was observed using UV-Vis Spectrophotometer. Bio-imaging of $Cs_3Bi_2I_9@SiO_2$ composites incorporated with L929 cells was monitored using an inverted fluorescence microscope under blue and green excitation. The results obtained from bio-imaging studies indicated that the $Cs_3Bi_2I_9@SiO_2$ nanocomposites entered the cell field and exhibited an emission under excitation. The non-toxic behavior of the synthesized $Cs_3Bi_2I_9@SiO_2$ composites was demonstrated using MTT cytotoxicity assay in L929 fibroblast mouse cell, which infers the viability of 97 % after 24 h.

Keywords: Materials science, nanostructures, halide perovskite, nanocomposite.

1. Introduction

Lead halide perovskites have achieved a favorable outcome in various applications such as solar cells, detectors, bioimaging, and light emitting diodes [1-3]. The rich properties of perovskite include tunable bandgap,[4-6] easy solution processability,[7-9] enhanced longevity,[10-11] high absorption coefficient,[12] improved electrons and hole mobility,[13,14] low exciton binding energy,[15] and lower density defects[16] were exploited to develop exceptional applications. But the risk of Pb toxicity has severely hindered the use of perovskites in the future. Despite their unprecedented remarkable progress and colossal expectation, the toxic behavior and material instability of Pb in the presence of light, water, and heat, restricts and prevents their possible uses applications and upcoming commercialization [17,18]. The development of lead-free perovskites would be significant yet demanding in future applications [19]. To retain the advantages of Pb-based perovskite materials, the elements following the sequence of Pb electronic configuration are recommended. As a result, various homovalent (such as Sn and Ge) and heterovalent (such as Bi, Sb, Cu, In, and Ag) elements have been used to replace Pb like Sn(II), Sn(IV), Ge(II), Bi(III), Sb(III), In(III), Ag(I), Cu(I), and Cu(II) have all been used as Pb substitutes at this point [20].

Lead-free halide perovskites (LFHP) are categorized into four groups based on their Pb^{2+} replacement strategies as $A_2B(I)B(III)X_6$, $AB(II)X_3$, $A_3B(III)_2X_9$, and new perovskite products [21]. Several less hazardous metals, such as Sn, Ge, Bi, and Sb, have been studied for developing lead-free perovskite materials. Bismuth-based halide perovskites have gained prime importance due to their stability and non-toxic nature. Because of its electronic configuration and ionic radius, stable bismuth (Bi) is a viable candidate for non-toxic and air-stable LFHPs compared to Sn and Ge [22]. Because of their +3 valence state, ternary Bi^{3+} -based perovskites are commonly constructed using the formula $A_3Bi_2X_9$, where A is a monovalent cation such as MA+, Cs+, or Ag+, and X is a halogen anion such as I^- or Br^-. Bi, a high atomic

number element with remarkable biocompatibility, is favorable to the human body. Whether in its pure elemental or compound form, Bi can significantly absorb near-infrared (NIR) light and subsequently transform that energy into heat, thereby acting as a photothermal agent [23]. Due to its favorable characteristics, such as low toxicity and ease of synthesis, bismuth-based nanoparticles are extensively researched in the detection and cancer therapy[24]. Additionally, Bi is a potential non-toxic replacement for Pb to develop quantum dots, photocatalysts, light emitters, and piezoelectric materials [25-33].$A_3Bi_2X_9$ perovskites are typically made up of two structures: a 0D dimer form of isolated face-sharing [B_2X_9] octahedra ($Cs_3Bi_2I_9$, $MA_3Bi_2I_9$, and $MA_3Sb_2I_9$) and a 2D layered perovskite. ($(NH_4)_3Sb_2I_9$, $MA_3Sb_2Cl_xI_9$, and $Rb_3Sb_2I_9$).[34-37] Optical and charge carrier characteristics, size, stability, structure, possible device applications, and toxicity are all aspects to consider when synthesizing halide perovskites.

Excellent research outputs in the halide perovskite materials are primarily employed for optoelectronic device constructions like hybrid photovoltaics and photodiodes. In contrast, the research focuses on exploiting halide perovskite nanocrystals for bio-imaging and medical applications which are not carried out much because of their instability against in aqueous medium[38,39]. Several methods are in practice to enhance the stability of perovskite nanocrystal, such as hydrophobic organic ligand coating, phospholipid micelles, moisture impermeable polymer embedding, and imparting super hydrophobic framework structure[40,41].

Research on drug delivery has significantly advanced due to the use of silica materials with advantageous nanostructures as drug carriers[42]. These enhancements include high pore volumes, the flexibility to customize the morphology and pore structure, vast surface areas, and superior biocompatibility, adjustable surface functionality, making silica materials as popular drug carriers. Silica nanoparticles have also been integrated into gene delivery through virus mimetic magnetic silica nanoclusters (VMSNCs)[43]. The present work is mainly directed towards $Cs_3Bi_2I_9$ and Cs3Bi2I9@SiO_2 shell layers having a narrow bandgap with green

emission from cell imaging with a fluorescence probe. Furthermore, this work has paved the way for the use of water-sensitive perovskite nanoparticles in a variety of biological applications.

An attempt has been made to develop single-phase $Cs_3Bi_2I_9$ perovskite nano-structured material using appropriate precursors, the facile synthetic process route, and the development of $Cs_3Bi_2I_9@SiO_2$ formation with different precursors. The $Cs_3Bi_2I_9$ perovskite and its silica composite are also characterized using other modern analytical methods. Data obtained from XRD, TEM, UV-Vis, luminescence, and MTT cytotoxicity are discussed, correlated, and reported.

2. Experimental

2.1. Materials

Cesium carbonate (Cs_2Co_3, 97%, SRL), bismuth iodide (BiI_3) pure (Otto, 99%), oleic acid (SRL, extra pure AR grade), oleylamine (SRL, 95%), 1-octadecene (Aldrich, 90%), tetraethyl orthosilicate (TEOS, regent grade 98%, Sigma-Aldrich) and (3-Aminopropyl) trimethoxy silane (TCI, Japan, 96%) were purchased and used without further purification. Hexane (SRL) was bought and dried using a molecular sieve at room temperature. For cell culture, DMEM (HiMedia), Penicillin, Streptomycin, Trypsin (Sigma Aldrich, EDTA solution), and MTT assay (EZ Count, HiMedia) were obtained from appropriate sources and used.

2.2. Synthesis of single-phase $Cs_3Bi_2I_9$:

$Cs_3Bi_2I_9$ halide perovskite was synthesized using an inert N_2 atmosphere in the glove box.

2.2.1. **Caesium Oleate formation procedure**:

Oleic acid and octadecene were added with the one mmol of cesium carbonate in a round-bottomed three-necked flask. The mixture was degassed for 30 min at 120 ℃. Then the temperature was raised to 140 ℃ and maintained for 6 h under an inert atmosphere. Finally,

the mixture was cooled down and stored in a nitrogen-filled glove box. The above prepared Cs-Oleate was preheated at 80 ℃ before use.

2.2.2. Hot injection synthesis of $Cs_3Bi_2I_9$ synthesis:

In a separate system, 0.15 mmol of bismuth (III) iodide (BiI_3) was added with oleic acid, 1-Octadecene, and Oleylamine in a 100 mL round-bottomed flask and was degassed at 110-120 ℃ for 30 min. The solution temperature gradually increased to 155 ℃ and was maintained for 20 min. Desired amount (1 (0.1 mmol), 1.5 (0.15 mmol), and 2 (0.20 mmol) mL) of preheated Cs-oleate was swiftly injected into the reaction flask under nitrogen atmosphere and kept for 1-10 min. Subsequently, the reaction mixture was cooled down with the ice bath, and the solution was collected for centrifugation. The supernatant was discarded and dispersed in hexane. The synthesis route has been optimized with varying the parameters like experimental temperature, the molar ratio of precursors, and growth period[44,45]. It was observed that the 0.1 and 0.15 mmole precursor solutions produced the best results with a 10 min growth period at 155 °C, and the details are presented in Table 1.

2.2.3. $Cs_3Bi_2I_9$ @ SiO_2 capping

Silica capping around $Cs_3Bi_2I_9$ particle was tried in two different ways, one is based on TEOS, and another is (3-Aminopropyl) trimethoxysilane. The silica coating (capping) on $Cs_3Bi_2I_9$ was carried out by *in situ* injection of 200 µL TEOS followed m-cresol (100 µL) at 80 ^{0}C after a 5 min growth period of the $Cs_3Bi_2I_9$ particle. Another type of SiO_2 was an attempt with 200 µL (3-Aminopropyl) trimethoxysilane without m-cresol injection with a 10 min growth period of $Cs_3Bi_2I_9$. The obtained crude product was centrifuged at 4500 rpm for 5min. Furthermore, it dispersed in the hexane solvent and dried for further analysis.

Table 1. Optimization of synthesis conditions for $Cs_3Bi_2I_9$ nanoparticles.

S. No.	Synthesis of $Cs_3Bi_2I_9$ - Optimization of parameters	BiI_3	Cs-Oleate volume (mL)	Growth period (min)	Temperature (^0C)
01	Growth period	0.15 mmol	1.5 (0.15 mmol)	30	155
			1.5 (0.15 mmol)	2	155
			1.5 (0.15 mmol)	5	155
			1.5 (0.15 mmol)	**10**	**155**
02	Growth temperature variation with period		1.5 (0.15 mmol)	1	185
			1.5 (0.15 mmol)	3	175
			1.5 (0.15 mmol)	5	165
			1.5 (0.15 mmol)	**10**	**155**
03	Cesium oleate precursor volume change		2.0 (0.20 mmol)	10	155
			1.5 (0.15 mmol)	10	155
			1.0 (0.10 mmol)	**10**	**155**
04	Variation of temperature with 1 mL precursor (0.10 mmol)		1 .0 (0.10 mmol)	10	165
			1 .0 (0.10 mmol)	10	173
			1 .0 (0.10 mmol)	10	183
			1.0 (0.10 mmol)	**10**	**155**

2.3.4. Characterization of synthesized $Cs_3Bi_2I_9$ and $Cs_3Bi_2I_9$@SiO_2

The phase purity of synthesized $Cs_3Bi_2I_9$ and $Cs_3Bi_2I_9$@SiO_2 was observed using 'X'PERT PANalytical powder X-ray diffraction (2°/min scan rate and 10° to 60° 2θ range). Jasco V-570 UV–vis–NIR spectrophotometer was used to record the UV-VIS spectrum of synthesized nanoparticles. Shimadzu fluorescence spectrophotometer confirmed the emission capability of synthesized pure and silica capped $Cs_3Bi_2I_9$ nanoparticles. Morphology and

elemental composition of synthesized $Cs_3Bi_2I_9$ and $Cs_3Bi_2I_9@SiO_2$ particles were confirmed using JEOL TEM 2100F high-resolution transmission electron microscopy (HRTEM).

2.3. Bioimaging studies:

2.3.1. Cell culture studies:

Fibroblast cells (L929) were grown in DMEM medium, which is enriched with FBS (10%), penicillin (100 units/mL), and Streptomycin (100 mg/mL) and was incubated under a 5% CO_2 atmosphere at 37 °C. Once after 80% cell confluence, base cells were detached from the plate with the help of trypsin and were seeded for further requirements.

2.3.2. Viability assay:

Cytotoxicity behavior of the $Cs_3Bi_2I_9@SiO_2$ perovskite samples developed was evaluated by MTT assay. The control groups were formed with pure L929 cells considered for 100% cell viability. The fibroblast cells were harvested (5×10^4 cells/well) and seeded in 96-well plates (Himedia, Mumbai, India) and incubated with 5% CO_2 at 37 °C for the cells to adhere to the wells. The medium was replaced with fresh medium containing compounds to determine its biocompatibility. After 24 h of treatment, MTT dye (20 µL) was added and incubated for 4 h at dark. After incubation, formazan crystals were solubilized with DMSO (150 µL). The absorbance of formazan in each well was monitored under 570 nm excitation using Thermo Scientific Multiskan™ GO Microplate Spectrophotometer (USA).

2.3.3. Cellular uptake:

Fluorescence inverted phase-contrast microscopy was used to visualize the uptake of compounds by cells. The fibroblast cells were seeded (1×10^4 cells/well) in a 96 well plate and incubated with DMEM complete medium for 24 h. The silica capped halide perovskite sample was added to the culture medium with the 10 mg and 50 mg concentrations of nanocomposite and incubated for 4 h. After incubation, the cells were carefully washed with phosphate-buffered saline twice to remove the unbounded dead and floated cells. In an inverted

fluorescence phase-contrast microscope (Nikon T*i*2-U, Japan), well-attached cells were observed for fluorescence under blue and green excitation. A schematic diagram of $Cs_3Bi_2I_9$ and $Cs_3Bi_2I_9@SiO_2$ synthesis and bioimaging is presented in Figure 1.

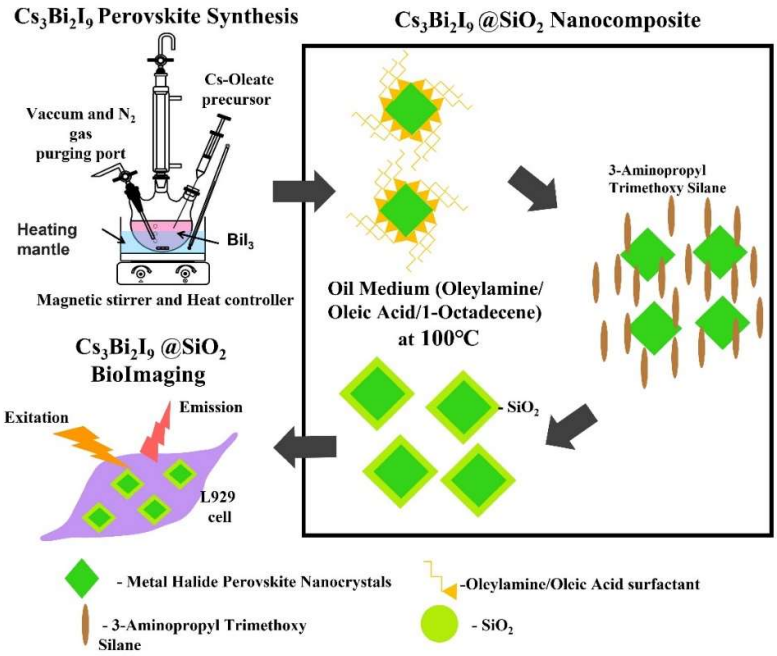

Figure 1. Schematic diagram of $Cs_3Bi_2I_9$ and $Cs_3Bi_2I_9@SiO_2$ and bioimaging.

3. Results and Discussion

3.1. XRD analysis

Data obtained from XRD patterns of the samples synthesized with different growth parameters like varying growth period, temperature, the molar ratio of precursor, and concentration of SiO_2 capping with two different methods are compared to find the optimal growth conditions. The XRD patterns recorded for 1.5 mL Cs-OA at 155 °C for different growth periods are presented in Figure 2. After oleate precursor injection, the changing growth period, viz., 30 sec, 2, 5, and 10 min., was maintained to optimize the time required to obtain single-phase $Cs_3Bi_2I_9$. The results confirmed that the growth period (10 min) with a 1:1 precursor (0.15 mmol) at 155 °C results in a single phase of $Cs_3Bi_2I_9$. The acquired pattern for the above growth parameter was well-matched with the hexagonal $Cs_3Bi_2I_9$ (JCPDS CARD

NO: 01-073-0707) without orthorhombic CsI (JCPDS CARD NO: 01-089-4257) mixed phase[46]. Rest all other growth periods having CsI phase mixing such as 30 sec and 2 min were showing almost 100% CsI phase and 5 min growth period leads little amount of $Cs_3Bi_2I_9$ phase when compared to that of CsI domination phase.

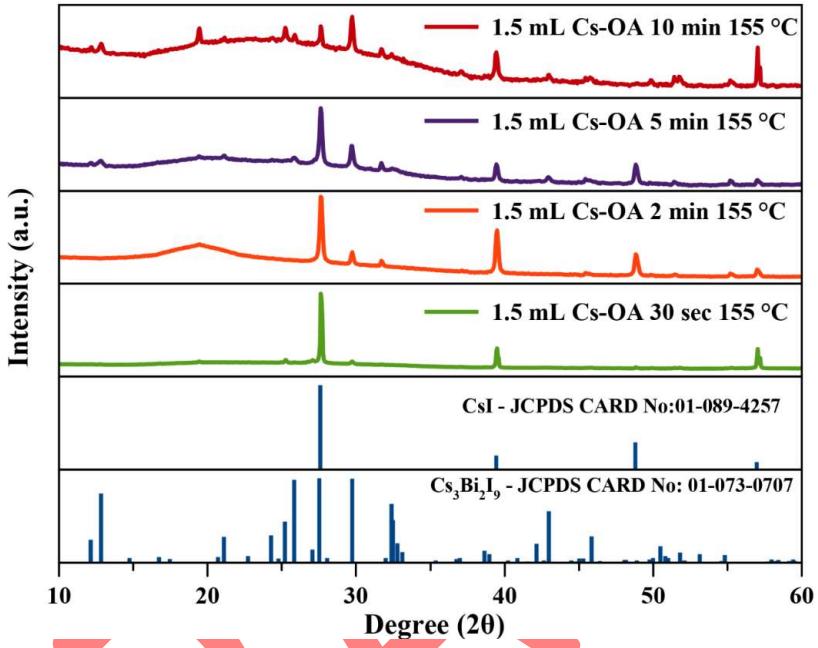

Figure 2. Comparative XRD patterns of $Cs_3Bi_2I_9$ nanoparticles upon changing growth period at constant precursor volume and temperature.

From the above results, a single phase of $Cs_3Bi_2I_9$ was achieved with a 1:1 precursor ratio under 155 °C temperature at a 10 min growth period, which drives curiosity to know the effects of other parameters. The temperature changes for the growth period were evaluated between 155 °C and 185 °C at 10 °C intervals (Figure 3). No significant impact was noticed from the XRD data for varying growth temperatures. Hence, it can be inferred that the growth temperature of 155 °C with a 10 min growth period is optimum for forming $Cs_3Bi_2I_9$. Instead of the single-phase $Cs_3Bi_2I_9$, CsI was formed due to an increase in temperature and a decrease in the growth period. Thus results confirm that Cs3Bi2I9 single-phase formation is predominantly reliant on the growth period.

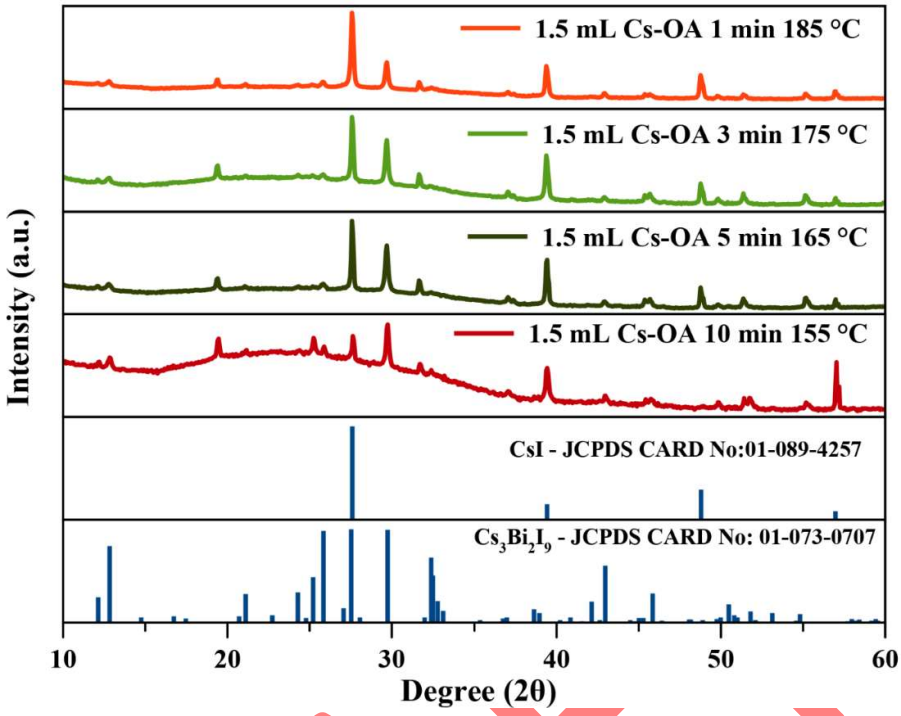

Figure 3. Comparative XRD patterns of $Cs_3Bi_2I_9$ nanoparticles upon changing temperature and growth period at constant precursor volume.

With optimized growth period (10 min) and temperature (155 ℃), cesium precursor volume was changed with 1:1.5, 1:1, and 2:1.5 (Cs-oleate: BiI_3) ratios to determine which ratio is most suitable for synthesizing single-phase $Cs_3Bi_2I_9$. Figure 4 reports the results of the changing precursor volume at constant temperature and growth period. XRD patterns indicate that 1:1.5 and 1:1 are more favorable molar ratios for achieving single-phase $Cs_3Bi_2I_9$. An increasing cesium content in the growth solution facilitates the formation of CsI instead of single-phase $Cs_3Bi_2I_9$, and reduced cesium in the solution leads to single-phase growth.

Surprisingly, the reduced cesium environment (1:1.5 mole ratio) helped cesium-rich $Cs_3Bi_2I_9$ synthesize, which was further investigated with different growth temperatures. The recorded reflections were compared in Figure 5; the chosen temperatures are 155, 165, 175, and 185 °C. It was observed that an enhancement of temperature did not influence the formation of the CsI phase, and the single phase of $Cs_3Bi_2I_9$ was maintained with the temperature change.

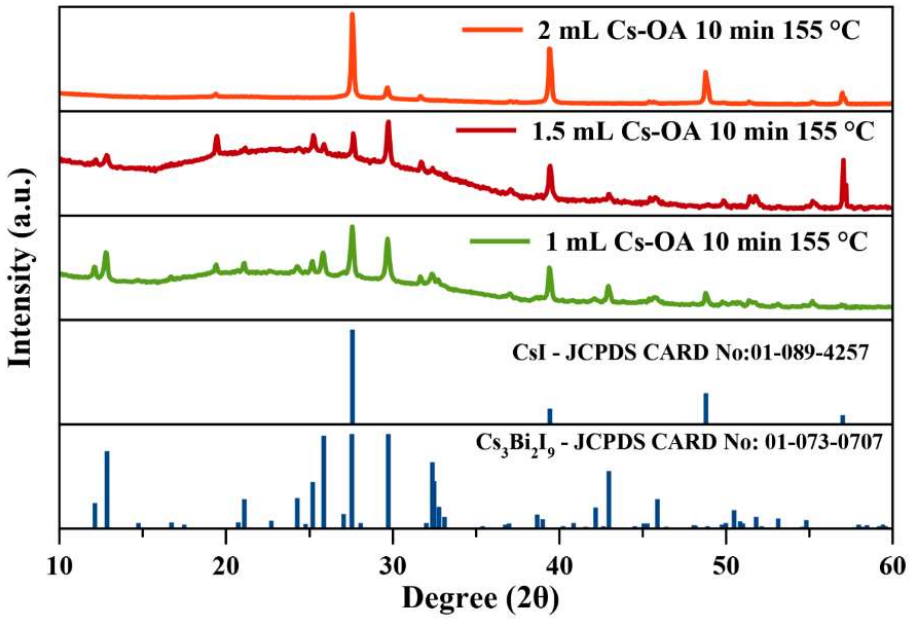

Figure 4. Comparative XRD patterns of $Cs_3Bi_2I_9$ nanoparticles upon changing precursor volume at constant temperature and growth period.

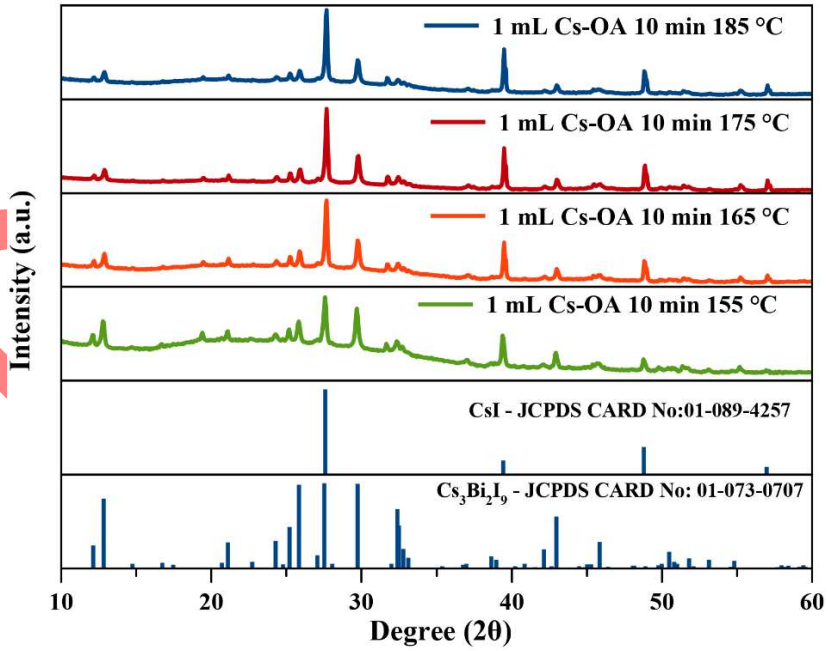

Figure 5. Comparative XRD patterns of $Cs_3Bi_2I_9$ nanoparticles upon changing growth temperature at constant precursor volume and growth period.

The single-phase $Cs_3Bi_2I_9$ growth around SiO_2 core-shell nanostructure was documented with XRD (Figure 6); the obtained patterns confirm the formation of $Cs_3Bi_2I_9$@SiO_2 without changing its phase.

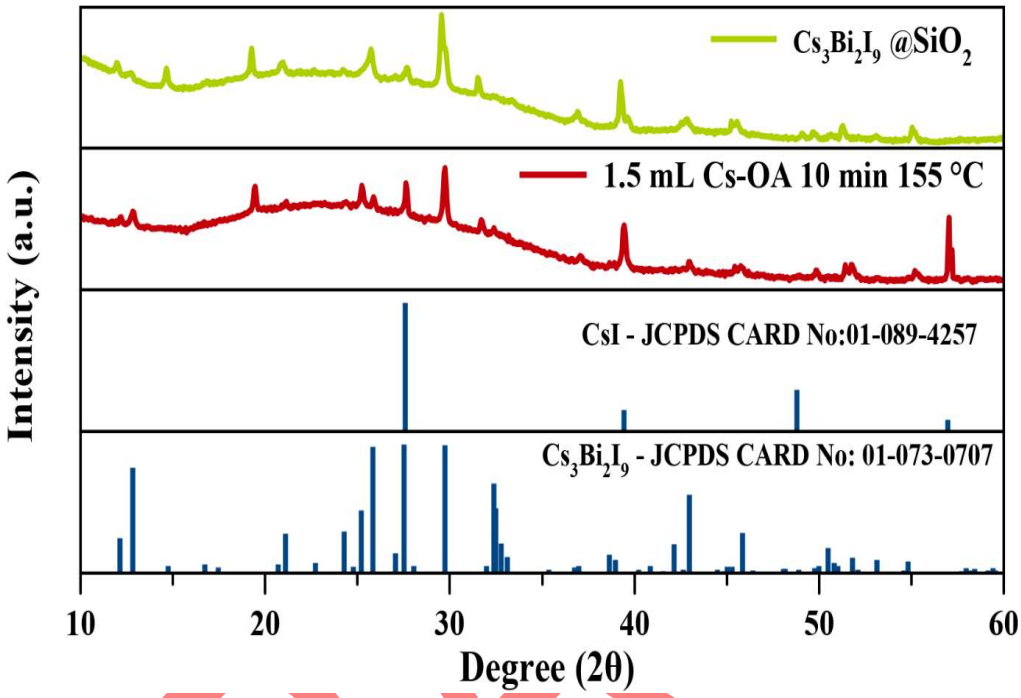

Figure 6. Comparative XRD patterns of $Cs_3Bi_2I_9$ and $Cs_3Bi_2I_9$@SiO_2 nanoparticles.

3.2. UV-Vis Spectroscopy

Figure 7 shows the comparative UV-Vis-IR absorption spectra of samples of $Cs_3Bi_2I_9$ (1.5 ml Cs-OA/155 °C) obtained during different time intervals of 30 sec, 2, 5, and 10 min. Like XRD results, UV-Vis-NIR spectra indicate the formation of $Cs_3Bi_2I_9$ single phase, which has gradually appeared while increasing the growth period. For 30 sec growth, there are no absorption peaks such as 282, 349, 433, and 503 nm region. A flat curve was observed for 30-sec growth, suggesting that the obtained curve is for CsI. While increasing the growth period, peak intensity increased and reached optimal intensity for a 10 min growth period. Observed 503 nm (2.56 eV) peak absorption infers the localized exciton transition raised from isolated $Br_2I_9^{3-}$ cluster in the $Cs_3Bi_2I_9$ phase. Sub bands such as 433 and 349 nm may be ascribed to electronic transition from ground state $^1S_0$ to the excited states of Bi^{3+} in isolated bismuth iodide

clusters[47,48]. Figure 8 presents the UV-Vis spectra at 155, 165, 175, and 185 °C, respectively, with 1 mL Cs-OA and a 10 min growth period. The well-defined and narrower peaks at 230 nm eventually appear to broaden upon thermal treatment up to 185 °C. From the results obtained, the temperature range between 155 and 185 °C is considered favorable for forming $Cs_3Bi_2I_9$. However, the optimum threshold temperature of 155 °C is sufficient to obtain the perovskite.

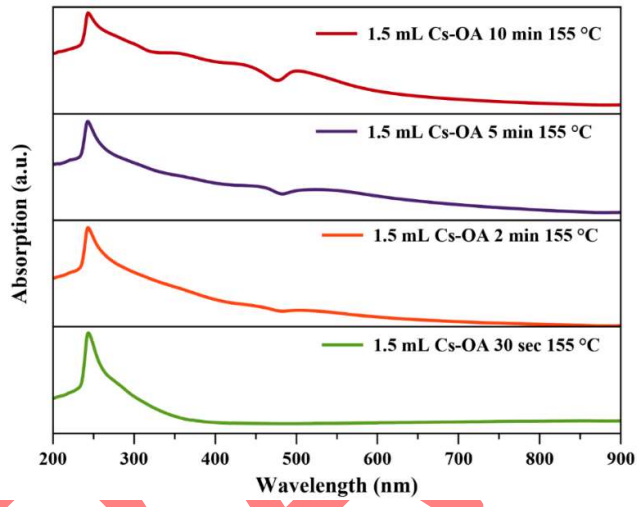

Figure 7. Comparative UV-VIS-IR absorption spectra of $Cs_3Bi_2I_9$ nanoparticles upon changing growth period at constant precursor volume and temperature.

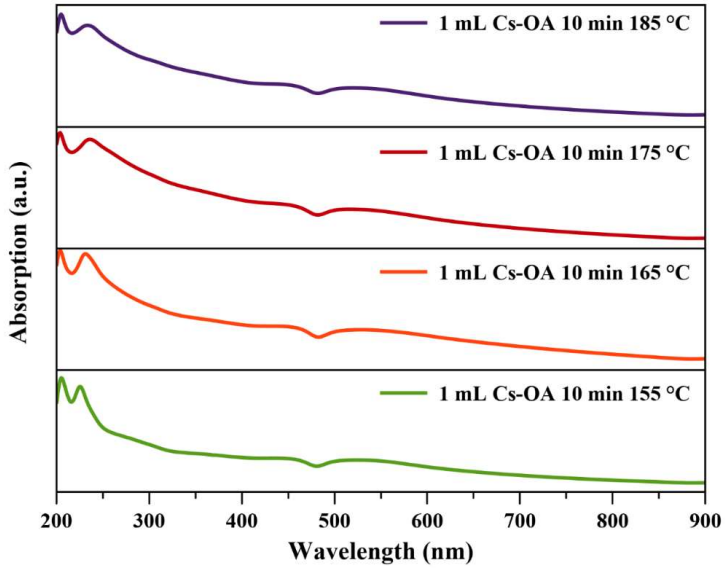

Figure 8. Comparative UV-VIS-IR absorption spectra of $Cs_3Bi_2I_9$ nanoparticles upon

changing growth temperature at constant precursor volume and growth period.

3.3. Emission Spectra

Figure 9 provides the comparative emission spectra of $Cs_3Bi_2I_9$ excited at 360 nm and $Cs_3Bi_2I_9$@SiO_2 nanoparticles excited at different excitation levels, viz., 380 nm, 400 nm 420 nm. Pure $Cs_3Bi_2I_9$ shows two other broad emissions, 469 and 621 nm, at an excitation wavelength of 360 nm. Different excitation was tried to find the emission pattern of $Cs_3Bi_2I_9$@SiO_2, which indicates an additional peak at 577 nm along with 469 and 621 broad emissions[49,50]. While increasing the excitation wavelength, there is not much shift observed for wide 469 and 621 nm emissions, but 577 nm is shifting to 606 and 636 nm upon 400 and 420 nm excitation, respectively. The additional peak 577 nm appearance with broad 621nm emission indicates emission from the direct and indirect bandgap of $Cs_3Bi_2I_9$.

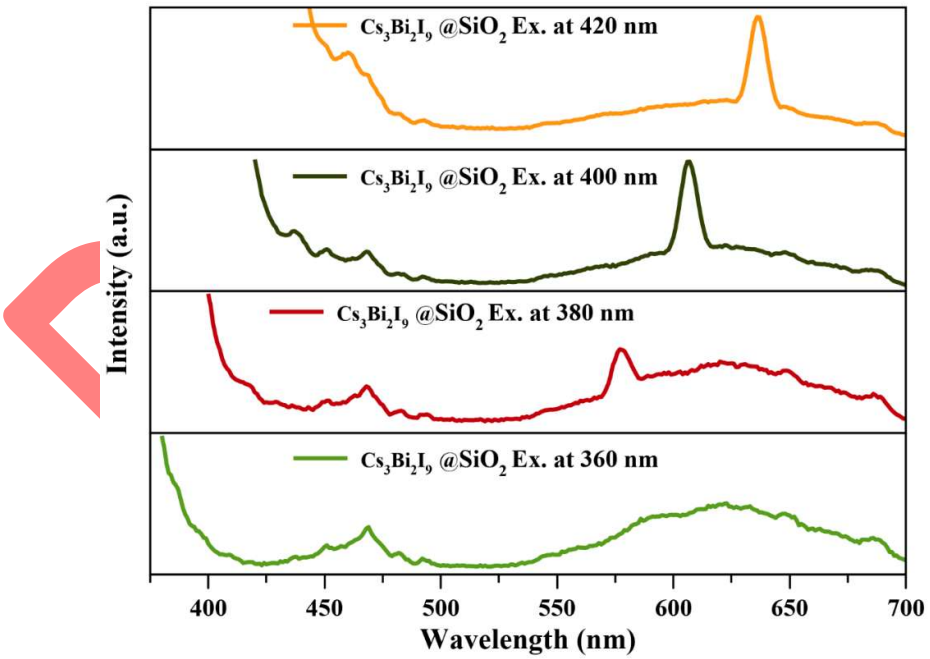

Figure 9. Comparative emission spectra of $Cs_3Bi_2I_9$ and $Cs_3Bi_2I_9$@SiO_2 nanoparticles under different excitations.

3.4. TEM and EDX Analysis

The morphology of $Cs_3Bi_2I_9$ was studied to know about the formation of mixed phases in an earlier growth period (1.5 mL Cs-OA/5 min/155 °C) and the images obtained are presented in Figures 10 (a-d). The morphology of synthesized $Cs_3Bi_2I_9$ and CsI mixed nanocrystals was a sheet-like structure, and the shape of the sheets is not well-formed, which shows uneven size uniformity. The results indicate that the growth period was insufficient to get any specified morphology; some are spheres in shape, and some are in bigger sheets. The interplanar distance obtained from HRTEM images is 0.73 nm, corresponding to the (100) plane of hexagonal Cs3Bi2I9 (Figure 10 c and d)[50].

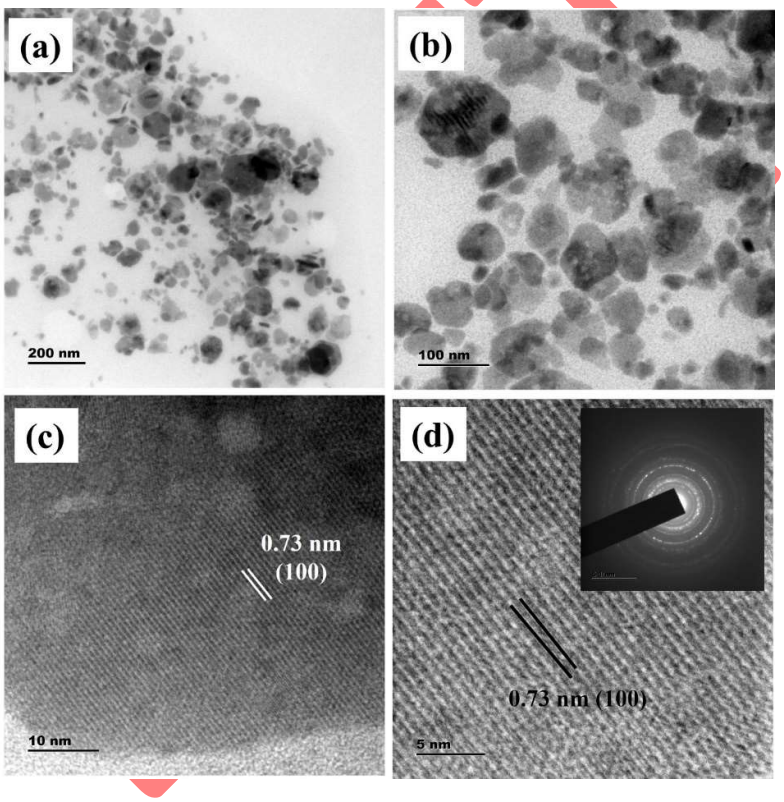

Figure 10. TEM and HRTEM images of $Cs_3Bi_2I_9$ (1.5 mL Cs-OA/5 min/155 °C).

Figure 11 (a-d) presents the TEM and HRTEM images of $Cs_3Bi_2I_9$ (1.5 ml Cs-OA/ 5 min/ 155 °C)@SiO_2 (TEOS-m-Cersol). The images of $Cs_3Bi_2I_9$@SiO_2 show uneven coating of SiO_2 appearing in the form of flakes and sheet-like clusters in SiO_2 foams. TEOS and the m-Cersol combination are not good for forming a uniform protection layer, resulting in big clusters.

HRTEM (Figure 11 (c and d)) indicates interplanar spacing of about 0.344 nm, which correlates to the (202) plane of hexagonal $Cs_3Bi_2I_9$.

Figure 12 (a-d) depicts the TEM images of $Cs_3Bi_2I_9$ (1.5 ml Cs-OA/ 10 min/ 155 °C). The images of square-shaped particles were observed with subangular edges for the sample obtained at a growth period of 10 min. This could be explained by transforming the spherical form into a square form of cubical structure over an extended growth period of 5 min to 10 min. SAED patterns of particles indicate that synthesized particles were single crystals in nature.

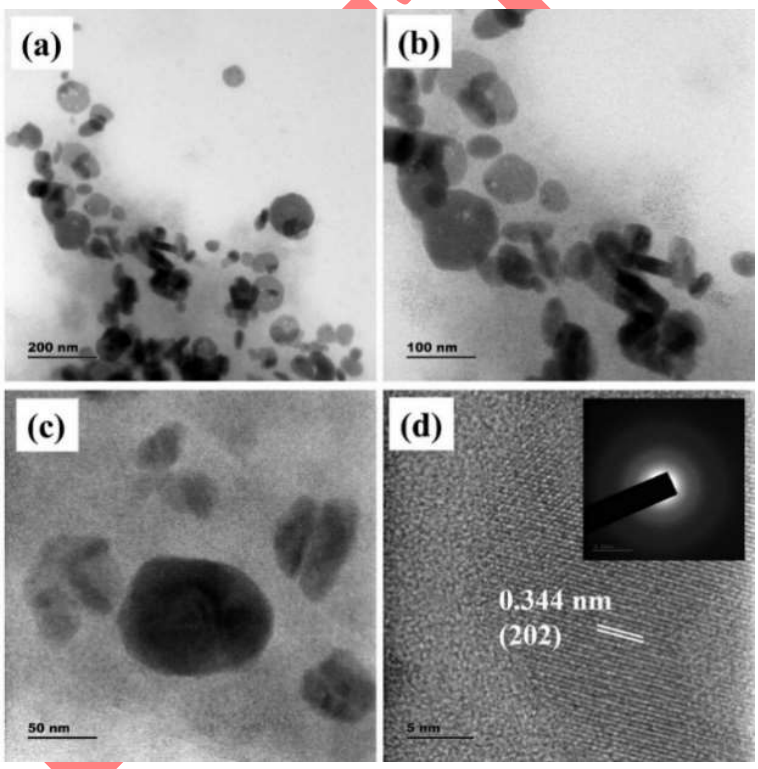

Figure 11. TEM and HRTEM images of $Cs_3Bi_2I_9$ (1.5 mL Cs-OA/5 min/155 °C) @SiO_2 (TEOS-m-Cersol).

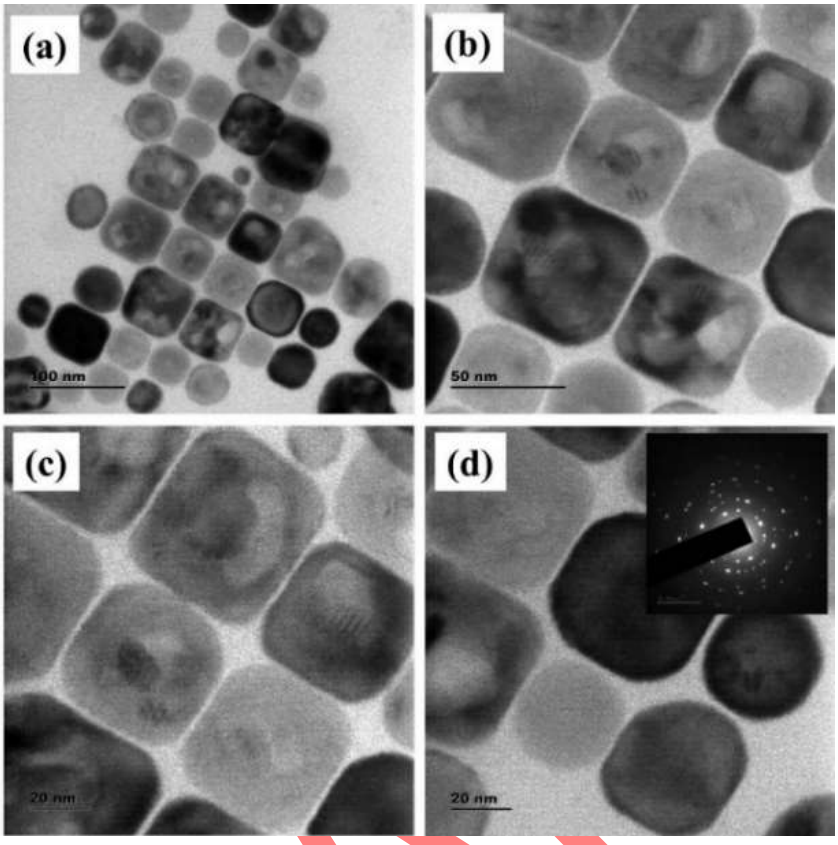

Figure 12. TEM images of $Cs_3Bi_2I_9$ (1.5 mL Cs-OA/10 min/155 °C).

Figure 13 (a-d) illustrates the TEM images of $Cs_3Bi_2I_9$ (1.5 ml Cs-OA/ 10 min/ 155ºC) @SiO_2 ((3-aminopropyl) triethoxy silane)). The images confirm that the formation of SiO_2 coating occurs effectively over the perovskite samples. An excellent thin layer of SiO_2 coating on $Cs_3Bi_2I_9$ was uniformly present for the samples obtained with 3-aminopropyltriethoxysilane. Thus, $Cs_3Bi_2I_9$ (1.5 ml Cs-OA/ 10 min/ 155ºC) @SiO_2 (TEOS-m-Cersol) shows better results than that of $Cs_3Bi_2I_9$ (1.5 ml Cs-OA/ 10 min/ 155ºC) @SiO_2 ((3-aminopropyl) triethoxy silane). The elemental composition of samples was confirmed from EDX analysis, which further ascertains the presence of elements viz., Cs, Bi, I, and Si in the prepared samples (Figure 14 (a-d)).

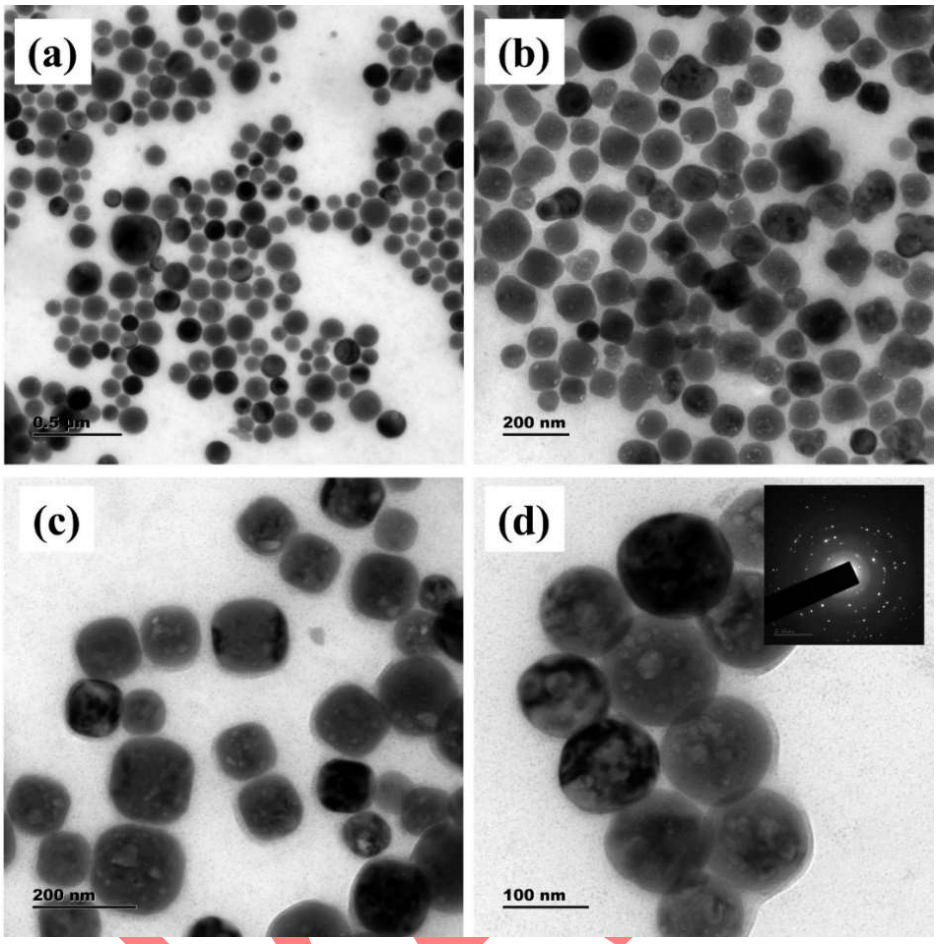

Figure 13. TEM images of $Cs_3Bi_2I_9$ (1.5 mL Cs-OA/10 min/155 °C) @SiO_2 (3-aminopropyltriethoxysilane).

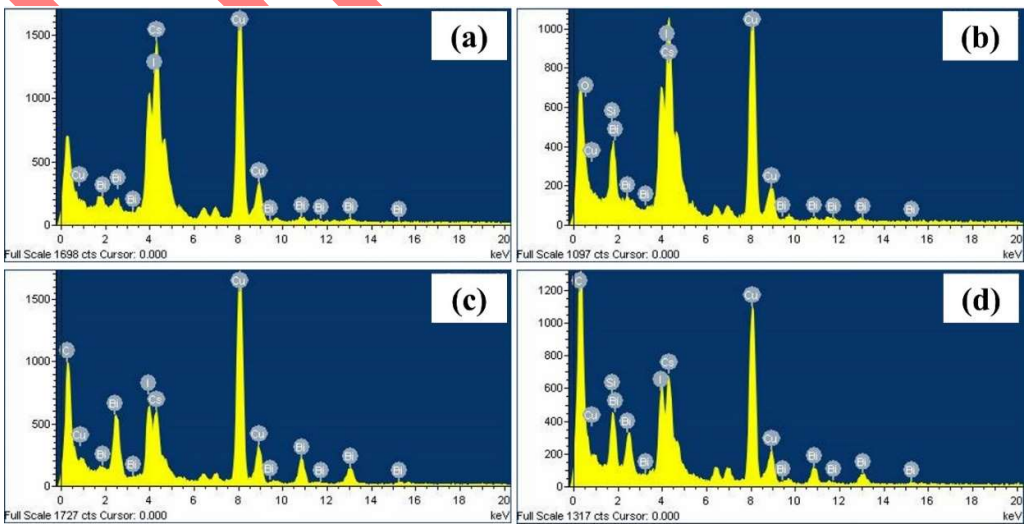

Figure 14. TEM images of $Cs_3Bi_2I_9$ (1.5 mL Cs-OA/5 min/155 °C) (a), $Cs_3Bi_2I_9$ (1.5 mL

Cs-OA/5 min/155 °C)@SiO_2 (TEOS-m-Cresol) (b), $Cs_3Bi_2I_9$ (1.5 mL Cs-OA/10 min/155 °C) (c), $Cs_3Bi_2I_9$ (1.5 mL Cs-OA/10 min/155 °C)@SiO_2 (3-aminopropyltriethoxysilane) (d).

From the TEM analysis, 5 min growth period is insufficient to complete the growth of $Cs_3Bi_2I_9$ and still secondary particles are present in the growth pot. This is the reason for finding uneven sized particles in the $Cs_3Bi_2I_9$ (1.5 mL Cs-OA/5 min/155 °C) samples. In Figure 12, $Cs_3Bi_2I_9$ (1.5 mL Cs-OA/10 min/155 °C) particle were monodispersed size and shape due to longer growth period and this sample posses no secondary particles.

3.5. Bioimaging and Cytotoxicity

Figure 15 presents the imaging of cultured bare L929 cells incubated with $Cs_3Bi_2I_9$ (1.5 ml Cs-OA/10 min/155 °C)@SiO_2((3-aminopropyl) triethoxy silane)) under blue and green excitations. Bare L929 cells excited at 450 nm and 510 nm show no significant emission, considered as control. L929 cells incubated with 10 mg of core-shell $Cs_3Bi_2I_9$@SiO_2 showed apparent emission, and bright spots indicated the cell particle presence. Adding 50 mg core-shell of Cs3Bi2I9@SiO2 incubated L929 cells shows the unmistakable outline of cell image and remarkable emission, indicating that the 50 mg of nanoparticle in the cells shows a sufficient amount for cell uptake for fluorescence bioimaging[51,52].

The cytotoxicity measurement of the synthesized samples was analyzed using an MTT assay kit. The viability of $Cs_3Bi_2I_9$@SiO_2 nanocomposites compared to healthy cells and the viability of nanocrystals was reported to be 97.83 %. The healthy cells ratio was calculated by comparing pure L929 cells with nanocomposite treated cells using the standardizing optical density method. Observed results indicate that prepared $Cs_3Bi_2I_9$@SiO_2 is compatible with L929 cells, and the obtained data were compared in Figure 16. Further, the cell morphology suggests that the nanocrystals are non-toxic to the cells and covered successfully with the SiO_2 layer.

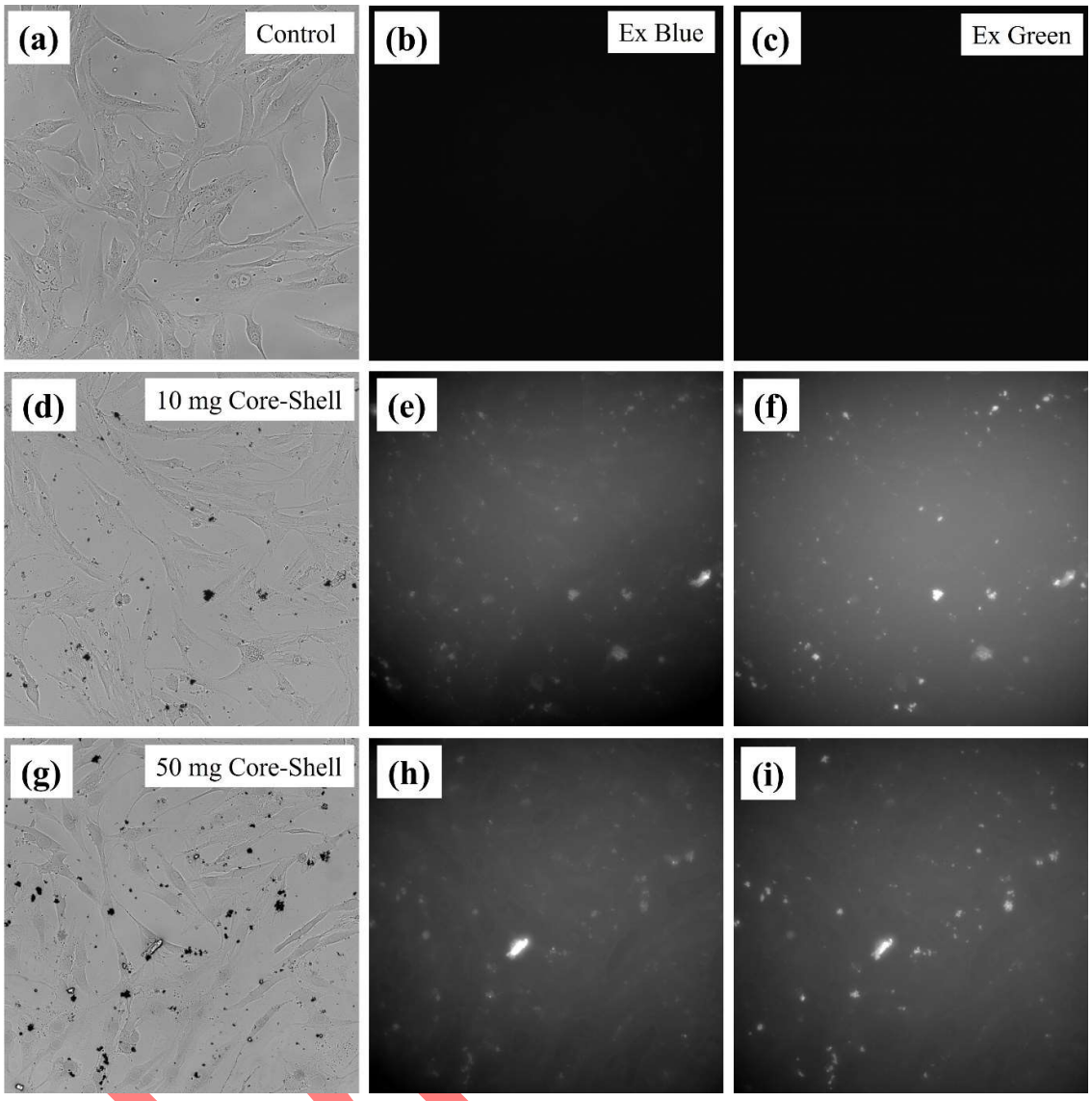

Figure 15. Microscopy images of Control (a, b and c), 10 mg (d, e and f) and 50 mg (g, h and i) of $Cs_3Bi_2I_9$ (1.5 mL Cs-OA/10 min/155 °C) @SiO_2 (3-aminopropyltriethoxysilane) added cancer cell under blue and green.

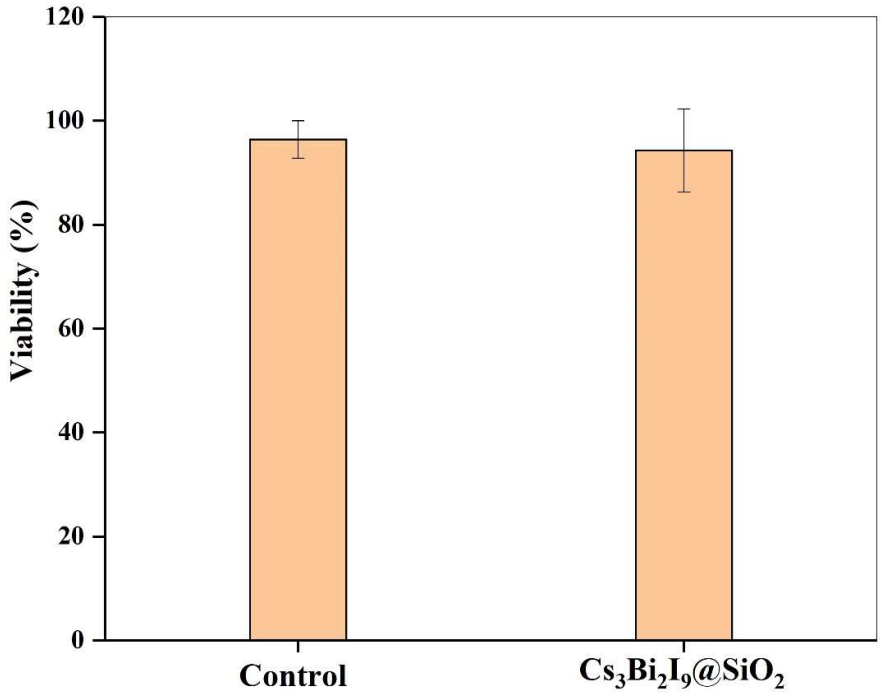

Figure 16. MTT cytotoxicity assay of $Cs_3Bi_2I_9$@SiO_2 nanoparticle viability.

4. **Conclusion**

The synthesis parameter for single-phase $Cs_3Bi_2I_9$ was successfully optimized using a high-temperature wet chemical method. From the obtained results, the optimal growth parameter to harvest single-phase is the 1:1 and 1.5:1 (Cs-oleate:BiI3) precursor ratio between Cs-oleate and BiI3 at 155 °C for 10 min growth period $Cs_3Bi_2I_9$. A thin layer of SiO_2 embedded $Cs_3Bi_2I_9$ is successfully synthesized using the *in situ* hot injection growth technique with (3-Aminopropyl) trimethoxy silane silica source. Precursor ratio, period, and temperature-dependent structural changes were recorded, and single-phase hexagonal $Cs_3Bi_2I_9$ was verified with XRD analysis. Increased absorption in the visible region while phase change from CsI to Cs3Bi2I9 was recorded, which agrees with XRD results. In luminescence analysis, the broad

blue and greenish-red emission of $Cs_3Bi_2I_9$ and $Cs_3Bi_2I_9@SiO_2$ was observed. The cytotoxicity assay studied using the L929 bone marrow cell line indicated that the $Cs_3Bi_2I_9@SiO_2$ samples possess non-toxic behavior with a viability of 97 %. The fluorescent images obtained with $Cs_3Bi_2I_9@SiO_2$ samples suggest that the perovskite materials developed in the present work can be considered biocompatible for fluorescence probes in various biomedical applications.

Acknowledgment

The author (D. Thangaraju) sincerely thanks the Science and Engineering Research Board (ECR/2017/002974), Department of Science and Technology, Government of India, for the financial support. The authors from KKU would like to express their gratitude to Deanship of Scientific Research at King Khalid University for funding this work through Research Groups Program under Grant No. R.G.P.2/123/43.

Declaration of conflict of interest: Authors have none to declare.

Data availability statement

The raw/processed data required to reproduce these findings cannot be shared at this time as the data also forms part of an ongoing study.

Credit Author Statement

Santhana Vedi Thangaraju Dheivasigamani Govarthini Seerangan Selvam, Takashi Kawakami, Narmadha Rajeswaran, Selvakumar Rajendran, Alagar Muthukaruppan: Conceptualization, Methodology, Investigation, Writing – Original Draft, Writing – Review & Editing and Funding acquisition. ***F. Maiz, Mohd. Shkir*:** Writing – Review & Editing, Review and Validation and Funding acquisition.

References

[1] W. Xu, Q. Hu, S. Bai, C. Bao, Y. Miao, Z. Yuan, T. Borzda, A.J. Barker, E. Tyukalova, Z. Hu, M. Kawecki, H. Wang, Z. Yan, X. Liu, X. Shi, K. Uvdal, M. Fahlman, W. Zhang, M. Duchamp, J.M. Liu, A. Petrozza, J. Wang, L.M. Liu, W. Huang, F. Gao, Rational molecular

passivation for high-performance perovskite light-emitting diodes, Nat. Photonics. 13 (2019) 418–424. https://doi.org/10.1038/s41566-019-0390-x.

[2] B. Pradhan, G. Sandeep Kumar, S. Sain, A. Dalui, U. Kumar Ghorai, S. Kumar Pradhan, S. Acharya, Size Tunable Cesium Antimony Chloride Perovskite Nanowires and Nanorods, Chem. Mater. 30 (2018) 2135–2142. https://doi.org/10.1021/acs.chemmater.8b00427.

[3] A. Kojima, K. Teshima, Y. Shirai, T. Miyasaka, Organometal Halide Perovskites as Visible-Light Sensitizers for Photovoltaic Cells, J. Am. Chem. Soc. 131 (2009) 6050–6051. https://doi.org/10.1021/ja809598r.

[4] M.M. Lee, J. Teuscher, T. Miyasaka, T.N. Murakami, H.J. Snaith, Efficient hybrid solar cells based on meso-superstructured organometal halide perovskites, Science. 338 (2012) 643–647. https://doi.org/10.1126/science.1228604.

[5] H. Zhao, Y. Han, Z. Xu, C. Duan, S. Yang, S. Yuan, Z. Yang, Z. Liu, S. Liu, A Novel Anion Doping for Stable CsPbI2Br Perovskite Solar Cells with an Efficiency of 15.56% and an Open Circuit Voltage of 1.30 V, Adv. Energy Mater. 9 (2019) 1902279. https://doi.org/10.1002/aenm.201902279.

[6] M. Abdi-Jalebi, Z. Andaji-Garmaroudi, S. Cacovich, C. Stavrakas, B. Philippe, J.M. Richter, M. Alsari, E.P. Booker, E.M. Hutter, A.J. Pearson, S. Lilliu, T.J. Savenije, H. Rensmo, G. Divitini, C. Ducati, R.H. Friend, S.D. Stranks, Maximizing and stabilizing luminescence from halide perovskites with potassium passivation, Nature. 555 (2018) 497–501. https://doi.org/10.1038/nature25989.

[7] E.H. Jung, N.J. Jeon, E.Y. Park, C.S. Moon, T.J. Shin, T.Y. Yang, J.H. Noh, J. Seo, Efficient, stable and scalable perovskite solar cells using poly(3-hexylthiophene), Nature. 567 (2019) 511–515. https://doi.org/10.1038/s41586-019-1036-3.

[8] Q. Jiang, Z. Ni, G. Xu, Y. Lin, P.N. Rudd, R. Xue, Y. Li, Y. Li, Y. Gao, J. Huang, Interfacial Molecular Doping of Metal Halide Perovskites for Highly Efficient Solar Cells, Adv. Mater. 32 (2020) 2001581. https://doi.org/10.1002/adma.202001581.

[9] M. Saliba, T. Matsui, K. Domanski, J.Y. Seo, A. Ummadisingu, S.M. Zakeeruddin, J.P. Correa-Baena, W.R. Tress, A. Abate, A. Hagfeldt, M. Grätzel, Incorporation of rubidium cations into perovskite solar cells improves photovoltaic performance, Science. 354 (2016) 206–209. https://doi.org/10.1126/science.aah5557.

[10] Q. Dong, Y. Fang, Y. Shao, P. Mulligan, J. Qiu, L. Cao, J. Huang, Electron-hole diffusion lengths > 175 μm in solution-grown CH3NH3PbI3 single crystals, Science. 347 (2015) 967–970. https://doi.org/10.1126/science.aaa5760.

[11] D.W. DeQuilettes, S.M. Vorpahl, S.D. Stranks, H. Nagaoka, G.E. Eperon, M.E. Ziffer, H.J. Snaith, D.S. Ginger, Impact of microstructure on local carrier lifetime in perovskite solar cells, Science. 348 (2015) 683–686. https://doi.org/10.1126/science.aaa5333.

[12] A. Bag, R. Radhakrishnan, R. Nekovei, R. Jeyakumar,Effect of absorber layer, hole transport layer thicknesses, and its doping density on the performance of perovskite solar cells by device simulation, Sol. Energy, 196 (2020) 177-182, https://doi.org/10.1016/j.solener.2019.12.014.

[13] J. Tong, Z. Song, D.H. Kim, X. Chen, C. Chen, A.F. Palmstrom, P.F. Ndione, M.O. Reese, S.P. Dunfield, O.G. Reid, J. Liu, F. Zhang, S.P. Harvey, Z. Li, S.T. Christensen, G. Teeter, D. Zhao, M.M. Al-Jassim, M.F.A.M. Van Hest, M.C. Beard, S.E. Shaheen, J.J. Berry, Y. Yan, K. Zhu, Carrier lifetimes of >1 ms in Sn-Pb perovskites enable efficient all-perovskite tandem solar cells, Science. 364 (2019) 475–479. https://doi.org/10.1126/science.aav7911.

[14] C.C. Stoumpos, C.D. Malliakas, M.G. Kanatzidis, Semiconducting tin and lead iodide perovskites with organic cations: Phase transitions, high mobilities, and near-infrared

photoluminescent properties, Inorg. Chem. 52 (2013) 9019–9038. https://doi.org/10.1021/ic401215x.

[15] L. M. Herz, Charge-Carrier Mobilities in Metal Halide Perovskites: Fundamental Mechanisms and Limits, ACS Energy Lett. 2 (2017) 1539–1548. https://doi.org/10.1021/acsenergylett.7b00276.

[16] J. Li, J. Duan, X. Yang, Y. Duan, P. Yang, Q. Tang, Review on recent progress of lead-free halide perovskites in optoelectronic applications, Nano Energy, 80 (2021) 105526. https://doi.org/10.1016/j.nanoen.2020.105526.

[17] C. Bi, X. Zheng, B. Chen, H. Wei, J. Huang, Spontaneous Passivation of Hybrid Perovskite by Sodium Ions from Glass Substrates: Mysterious Enhancement of Device Efficiency Revealed, ACS Energy Lett. 2 (2017) 1400–1406. https://doi.org/10.1021/acsenergylett.7b00356.

[18] M. Chen, M.G. Ju, A.D. Carl, Y. Zong, R.L. Grimm, J. Gu, X.C. Zeng, Y. Zhou, N.P. Padture, Cesium Titanium(IV) Bromide Thin Films Based Stable Lead-free Perovskite Solar Cells, Joule. 2 (2018) 558–570. https://doi.org/10.1016/j.joule.2018.01.009.

[19] Y. Gao, Y. Pan, F. Zhou,G. Niu, C. Yan, Lead-free halide perovskites: a review of the structure–property relationship and applications in light emitting devices and radiation detectors, J. Mater. Chem. A, 9 (2021)2050-7488, http://dx.doi.org/10.1039/D1TA01737C

[20] M. Wang,W. Wang,B. Ma, W. Shen, L. Liu,K. Cao,S. Chen, W. Huang, Wei, Lead-Free Perovskite Materials for Solar Cells, Nano-Micro Letters, 13 (2021) 2150-5551, https://doi.org/10.1007/s40820-020-00578-z

[21] Y. Li, Z. Shi,W. Liang, J. Ma, X. Chen, D. Wu,Y. Tian, X. Li, C. Shan, X. Fang, Recent advances toward environment-friendly photodetectors based on lead-free metal halide

perovskites and perovskite derivatives, Mater. Horiz. 8 (2021) 2051-6347, http://dx.doi.org/10.1039/D0MH01567A

[22] J. Li, J. Duan, X. Yang, Y. Duan, P. Yang, Q. Tang, Review on recent progress of lead-free halide perovskites in optoelectronic applications, Nano Energy, 80 (2021) 2211-2855, https://doi.org/10.1016/j.nanoen.2020.105526

[23] S. Wen, M. Ovais, X. Li, J. Ren, T. Liu,Z. Wang, R. Cai, C. Chen, Tailoring bismuth-based nanoparticles for enhanced radiosensitivity in cancer therapy, Nanoscale, 14 (2022) 2040-3364, http://dx.doi.org/10.1039/D2NR01500E

[24] L. Li, Y. Lu, Z. Lin, A.S. Mao, J. Jiao, Y. Zhu, C. Jiang, Z. Yang, M. Peng, C. Mao, Ultralong tumor retention of theranostic nanoparticles with short peptide-enabled active tumor homing, Mater. Horiz. 6 (2019) 2051-6347, http://dx.doi.org/10.1039/C9MH00014C

[25] Z. Li, C. Zhang, B. Li, C. Lin, Y. Li, L. Wang, R.J. Xie, Large-scale room-temperature synthesis of high-efficiency lead-free perovskite derivative (NH4)2SnCl6:Te phosphor for warm wLEDs, Chem. Eng. J. 420 (2021) 129740. https://doi.org/10.1016/j.cej.2021.129740.

[26] J. Zhou, J. Luo, X. Rong, P. Wei, M.S. Molokeev, Y. Huang, J. Zhao, Q. Liu, X. Zhang, J. Tang, Z. Xia, Lead-Free Perovskite Derivative Cs 2 SnCl 6−x Br x Single Crystals for Narrowband Photodetectors, Adv. Opt. Mater. 7 (2019) 1900139. https://doi.org/10.1002/adom.201900139.

[27] A.A. Hussain, A.K. Rana, M. Ranjan, Air-stable lead-free hybrid perovskite employing self-powered photodetection with an electron/hole-conductor-free device geometry, Nanoscale. 11 (2019) 1217–1227. https://doi.org/10.1039/c8nr08959k.

[28] X.G. Zhao, D. Yang, J.C. Ren, Y. Sun, Z. Xiao, L. Zhang, Rational Design of Halide Double Perovskites for Optoelectronic Applications, Joule, 2 (2018) 1662-1673. https://doi.org/10.1016/j.joule.2018.06.017.

[29] H. Zhou, X. Liu, G. He, L. Fan, S. Shi, J. Wei, W. Xu, C. Yuan, N. Chai, B. Chen, Y. Zhang, X. Zhang, J. Zhao, X. Wei, J. Yin, D. Tian, Synthesis, Crystal Structure, UV–Vis Adsorption Properties, Photoelectric Behavior, and DFT Computational Study of All-Inorganic and Lead-Free Copper Halide Salt K2Cu2Cl6, ACS Omega. 3 (2018) 14021–14026. https://doi.org/10.1021/acsomega.8b01337.

[30] Y. Li, Z. Shi, W. Liang, J. Ma, X. Chen, D. Wu, Y. Tian, X. Li, C. Shan, X. Fang, Recent advances toward environment-friendly photodetectors based on lead-free metal halide perovskites and perovskite derivatives, Mater. Horizons. 8 (2021) 1367–1389. https://doi.org/10.1039/d0mh01567a.

[31] B.W. Park, B. Philippe, X. Zhang, H. Rensmo, G. Boschloo, E.M.J. Johansson, Bismuth Based Hybrid Perovskites A3Bi2I9 (A: Methylammonium or Cesium) for Solar Cell Application, Adv. Mater. 27 (2015) 6806–6813. https://doi.org/10.1002/adma.201501978.

[32] L. Qiu, L.K. Ono, Y. Qi, Advances and challenges to the commercialization of organic–inorganic halide perovskite solar cell technology, Mater. Today Energy, 7 (2018) 169-189. https://doi.org/10.1016/j.mtener.2017.09.008.

[33] L. Chouhan, S. Ghimire, C. Subrahmanyam,T. Miyasaka, V. Biju, Synthesis, optoelectronic properties and applications of halide perovskites, Chem. Soc. Rev., 2020,49, 2869-2885 http://dx.doi.org/10.1039/C9CS00848A

[34] B.W. Park, B. Philippe, X. Zhang, H. Rensmo, G. Boschloo, E.M.J. Johansson, Bismuth Based Hybrid Perovskites A3Bi2I9 (A: Methylammonium or Cesium) for Solar Cell Application, Adv. Mater. 27 (2015) 6806–6813. https://doi.org/10.1002/adma.201501978.

[35] K. Eckhardt, V. Bon, J. Getzschmann, J. Grothe, F.M. Wisser, S. Kaskel, Crystallographic insights into (CH3NH3)3(Bi2I9): A new lead-free hybrid organic-inorganic material as a potential absorber for photovoltaics, Chem. Commun. 52 (2016) 3058–3060. https://doi.org/10.1039/c5cc10455f.

[36] C. Zuo, L. Ding, Lead-free Perovskite Materials (NH4)3Sb2IxBr9−x, Angew. Chemie - Int. Ed. 56 (2017) 6528–6532. https://doi.org/10.1002/anie.201702265.

[37] L. Chouhan, S. Ghimire, C. Subrahmanyam, T. Miyasaka, V. Biju, Synthesis, optoelectronic properties and applications of halide perovskites, Chem. Soc. Rev. 49 (2020) 2869–2885. https://doi.org/10.1039/c9cs00848a.

[38] K. Ken Chan, D. Giovanni, H. He, T. Chien Sum, K.-T. Yong, Water-Stable All-Inorganic Perovskite Nanocrystals with Nonlinear Optical Properties for Targeted Multiphoton Bioimaging, ACS Appl. Nano Mater. 4 (2021) 9022–9033. https://doi.org/10.1021/acsanm.1c01621.

[39] I.G. Koryakina, P.K. Afonicheva, K.V. Arabuli, A.A. Evstrapov, A.S. Timin, M.V. Zyuzin, Microfluidic synthesis of optically responsive materials for nano- and biophotonics, Adv. Colloid Interface Sci. 298 (2021) 102548, https://doi.org/10.1016/j.cis.2021.102548.

[40] C. Zhang, J. Chen, L. Kong, L. Wang, S. Wang, W. Chen, R. Mao, L. Turyanska, G. Jia, X. Yang, Core/Shell Metal Halide Perovskite Nanocrystals for Optoelectronic Applications, Adv. Funct. Mater. 31 (2021) 2100438. https://doi.org/10.1002/adfm.202100438.

[41] Z. Yang, J. Xu, S. Zong, S. Xu, D. Zhu, Y. Zhang, C. Chen, C. Wang, Z. Wang, Y. Cui, Lead Halide Perovskite Nanocrystals–Phospholipid Micelles and Their Biological Applications: Multiplex Cellular Imaging and in Vitro Tumor Targeting, ACS Appl. Mater. Interfaces. 11 (2019) 47671–47679. https://doi.org/10.1021/acsami.9b12924.

[42] S.J. Kim, Y. Choi, K.T. Min, S. Hong, Dexamethasone-Loaded Radially Mesoporous Silica Nanoparticles for Sustained Anti-Inflammatory Effects in Rheumatoid Arthritis. Pharmaceutics 2022, 14, 985. https://doi.org/10.3390/pharmaceutics14050985

[43] G. Naveen, D.D. Wang,Y. Zhu, C. Mao, Virus-Mimetic Cytoplasm-Cleavable Magnetic/Silica Nanoclusters for Enhanced Gene Delivery to Mesenchymal Stem Cells, Angew. Chem. 52, 2013 11278-11281, https://doi.org/10.1002/anie.201301113

[44] V. Santhana, Darius C. Greenidge, D. Thangaraju, R. Marnadu, T. Alshahrani, Mohd. Shkir, Synthesis and emission characteristics of lead-free novel Cs_4SnBr_6/SiO_2 nanocomposite, Materials Letters 280 (2020) 128562 https://doi.org/10.1016/j.matlet.2020.128562

[45] D Thangaraju, R Marnadu, V Santhana, A Durairajan, P Kathirvel, J Chandrasekaran, S Jayakumar, MA Valente, Darius C Greenidge, Solvent influenced synthesis of single-phase SnS 2 nanosheets for solution-processed photodiode fabrication, CrystEngComm, 22 (2020) 525-533 https://doi.org/10.1039/C9CE01417A

[46] S.E. Creutz, H. Liu, M. E. Kaiser, X. Li, D. R. Gamelin, Structural Diversity in Cesium Bismuth Halide Nanocrystals, Chem. Mater. 31 (2019) 4685–4697. https://doi.org/10.1021/acs.chemmater.9b00640.

[47] B. Bin Yu, M. Liao, J. Yang, W. Chen, Y. Zhu, X. Zhang, T. Duan, W. Yao, S.H. Wei, Z. He, Alloy-induced phase transition and enhanced photovoltaic performance: The case of Cs3Bi2I9-xBrx perovskite solar cells, J. Mater. Chem. A. 7 (2019) 8818–8825. https://doi.org/10.1039/c9ta01978b.

[48] G.M. Paternò, N. Mishra, A.J. Barker, Z. Dang, G. Lanzani, L. Manna, A. Petrozza, Broadband Defects Emission and Enhanced Ligand Raman Scattering in 0D Cs3Bi2I9 Colloidal Nanocrystals, Adv. Funct. Mater. 29 (2019) 1805299. https://doi.org/10.1002/adfm.201805299.

[49] J. Pal, A. Bhunia, S. Chakraborty, S. Manna, S. Das, A. Dewan, S. Datta, A. Nag, Synthesis and Optical Properties of Colloidal M3Bi2I9 (M = Cs, Rb) Perovskite Nanocrystals, J. Phys. Chem. C. 122 (2018) 10643–10649. https://doi.org/10.1021/acs.jpcc.8b03542.

[50] Y. Zhang, J. Yin, M. R. Parida, G. H. Ahmed, J. Pan, O. M. Bakr, J.-L. Brédas, O. F. Mohammed, Direct-Indirect Nature of the Bandgap in Lead-Free Perovskite Nanocrystals, J. Phys. Chem. Lett. 8 (2017) 3173–3177. https://doi.org/10.1021/acs.jpclett.7b01381.

[51] D. Thangaraju, Y. Masuda, I.K.M.M. Sahip, W. Inami, Y. Kawata and Y. Hayakawa, Multi-modal imaging of HeLa cells using a luminescent ZnS:Mn/$NaGdF_4$:Yb:Er nanocomposite with enhanced upconversion red emission, RSC Adv. 6 (2016) 33569-33579. https://doi.org/10.1039/C6RA02422J

[52] I.K.M.M. Sahip, A. Tanaka, D. Thangaraju, K. Sugimoto, Y. Shimura W. Inami Y. Kawata and Y. Hayakawa, Photothermally Active Upconversion Core–Shell $NaGdF_4$:Yb:Tm@Cu Nanostructures: Synthesis and Theranostic Properties, Part. Part. Syst. Char. 35 (2018) 1800227. https://doi.org/10.1002/ppsc.201800227